

Supporting information

# Design of a new Ni@NCNT/Graphene Hybrid Structured Catalyst for High-performance Electrochemical CO<sub>2</sub> Reduction: Unravelling the Role of N-doping

Jian Zhu<sup>a‡</sup>, Jing Hu<sup>c‡</sup>, Zhenyu Wang<sup>c</sup>, Zhouguang Lu<sup>c</sup>, Shoubhik Das<sup>a,b\*</sup>, Pegie Cool<sup>a\*</sup>

a) Department of Chemistry, University of Antwerp, Antwerp 2610, Belgium

b) Department of Chemistry, University of Bayreuth, 95447 Bayreuth, Germany

c) Department of Materials Science and Engineering, Shenzhen Key Laboratory of Interfacial Science and Engineering of Materials, Southern University of Science and Technology, Shenzhen 518055, PR China

‡These authors contribute equally: Jian Zhu, Jing Hu

Corresponding authors:

\*S. D. e-mail: [shoubhik.das@uni-bayreuth.de](mailto:shoubhik.das@uni-bayreuth.de)

\*P. C. e-mail: [pegie.cool@uantwerpen.be](mailto:pegie.cool@uantwerpen.be)

Experimental section .....	1
<b>1. Catalyst preparation</b> .....	1
1.1.1 Chemicals and products .....	1
1.2.1 Synthesis of bulk g-C <sub>3</sub> N <sub>4</sub> precursor. ....	1
1.2.2 Preparation of Ni@NCNT/Gr-T .....	1
1.2.3 Preparation of Ni@NCNT/Gr-xPVP .....	2
1.2.4 Preparation of Ni@NCNT/Gr-R catalyst .....	2
<b>2. Materials characterizations</b> .....	2
<b>2.1 ICP-MS measurements</b> .....	3
<b>2.2 Electrochemical measurements</b> .....	3
<b>3 Theoretical Calculations</b> .....	5
Supplementary Figures.....	7
<b>Figure S1.</b> Percentage of various deconvoluted D and G bands from Raman spectra..	7
<b>Figure S2.</b> a) N <sub>2</sub> adsorption-desorption isotherms, and b) Porosity distribution of the Ni@NCNT/Gr-T (T = 700, 800, 900 °C) catalysts.....	8
<b>Figure S3.</b> XPS survey spectra of Ni@NCNT/Gr-T (T = 700, 800, 900 °C) catalysts obtained at various temperatures.....	9
<b>Figure S4.</b> Percentages of pyridinic N, pyrrolic N, graphitic N, and oxidized N of the obtained Ni@NCNT/Gr-T (T = 700, 800, 900 °C) catalysts (based on XPS results).	10
<b>Figure S5.</b> <sup>1</sup> H NMR spectra of the 0.5 M KHCO <sub>3</sub> electrolyte after electrolysis for 24 h.....	11
<b>Figure S6.</b> LSV curves of Ni@NCNT/Gr-800 and NC at the scan rate of 10 mV s <sup>-1</sup> . .....	12
<b>Figure S7.</b> a) LSV curves of Ni@NCNT/Gr-800 and Ni@NCNT/Gr-800-48h at the scan rate of 10 mV s <sup>-1</sup> ; b) CO FE of Ni@NCNT/Gr-800 and Ni@NCNT/Gr-800-48h. ....	13
<b>Figure S8.</b> H <sub>2</sub> FE of the as-prepared catalysts Ni@NCNT/Gr-T (T = 700, 800, 900 °C) obtained at various temperatures.....	14
<b>Figure S9.</b> Cyclic voltammetry measurements for Ni@NCNT/Gr-T (T = 700, 800, 900 °C) at scan rates varying from 10 to 100 mV s <sup>-1</sup> . ....	15
<b>Figure S10.</b> a) XRD pattern, b) Raman spectra, c) N <sub>2</sub> adsorption-desorption isotherms, and d) Porosity distribution of the Ni@NCNT/Gr-xPVP (x = 1, 2, 3) catalysts obtained with different amounts of PVP (0.1 g, 0.2 g, 0.4 g). ....	16
<b>Figure S11.</b> ECO <sub>2</sub> RR performances of the Ni@NCNT/Gr-xPVP (x = 1, 2, 3) catalysts. a) LSV curves of the Ni@NCNT/Gr-xPVP catalysts in CO <sub>2</sub> saturated 0.5 M	

KHCO <sub>3</sub> at a scan rate of 10 mV s <sup>-1</sup> , b) and c) CO FEs and $j_{CO}$ at various potentials (Vs. RHE), d) Charging current density differences plotted against scan rates, roughness factor (RF) of Ni@NCNT/Gr-1PVP, Ni@NCNT/Gr-2PVP, Ni@NCNT/Gr-3PVP electrodes are 560, 805, and 605, respectively. ....	17
<b>Figure S12.</b> Cyclic voltammetry measurements for Ni@NCNT/Gr-xPVP (x = 1, 2, 3) at scan rates varying from 10 to 100 mV s <sup>-1</sup> . ....	18
<b>Figure S13.</b> a) and b) TEM and HRTEM image, c) SAED pattern, d) Particle size distribution, e) and f) elemental mapping of the as-prepared Ni@NCNT/Gr-R catalyst. ....	19
<b>Figure S14.</b> a) XRD pattern, b) Raman spectra, c) High resolution N 1s XPS spectra, d) High resolution Ni 2p XPS spectra of the Ni@NCNT/Gr-R catalyst. ....	20
<b>Figure S15.</b> a) TEM image, b) SAED pattern, d) HAADF image and d) Elemental mapping of Ni@NCNT/Gr-R after electrolysis at -0.71 V for 24 h. ....	21
<b>Figure S16.</b> Optimized calculation models of pyrrolic N-Gr/Ni, pyridinic N-Gr/Ni, and Graphitic N-Gr/Ni with different absorbates. ....	22
<b>Figure S17.</b> Optimized calculation models of pyrrolic N-Gr, Ni (111), and Graphitic N-Gr with different absorbates. ....	23
<b>Figure S18.</b> Optimized calculation models with absorbed *H. ....	24
<b>Figure S19.</b> a) The calculated free energy diagrams for ECO2RR to CO on graphene, pyrrolic N-doped graphene, and bare Ni. b) The calculated free energy diagrams for HER to H <sub>2</sub> on graphene, pyrrolic N-doped graphene, and bare Ni. ....	25
<b>Figure S20.</b> Limiting potential difference for ECO2RR and HER on Pyrrolic N-Gr/Ni, Pyridinic N-Gr/Ni, and Graphitic N-Gr/Ni. ....	26
<b>Table S1.</b> Comparison of ECO2RR performances with recently reported advanced catalysts in H-type cell. ....	27
<b>References</b> .....	28

# Experimental section

## 1. Catalyst preparation

### 1.1.1 Chemicals and products

All the chemicals were used as received.  $\text{Ni}(\text{NO}_3)_2 \cdot 6\text{H}_2\text{O}$  and polyvinyl pyrrolidone (PVP,  $M_r = 40,000 \text{ g mol}^{-1}$ ) were purchased from Sigma Chemical Company, Melamine was purchased from Sigma-Aldrich.  $\text{KHCO}_3$  and  $\text{HCl}$  were purchased from Acros Organics. Ethanol was purchased from VWR International, LLC.

### 1.2.1 Synthesis of bulk g- $\text{C}_3\text{N}_4$ precursor.

The g- $\text{C}_3\text{N}_4$  was synthesized according to the previous report by a thermal polymerization strategy.<sup>1, 2</sup> In detail, the 10 g melamine was heated from room temperature to 550 °C at the ramping rate of 2.3 °C  $\text{min}^{-1}$  in a muffle furnace and then maintained at that temperature under air atmosphere for 4 h. Finally, the light-yellow bulk g- $\text{C}_3\text{N}_4$  was obtained when it cooled down to room temperature naturally. The powder g- $\text{C}_3\text{N}_4$  was obtained by grounding bulk g- $\text{C}_3\text{N}_4$  in a mortar.

### 1.2.2 Preparation of Ni@NCNT/Gr-T

In this research, a series of Ni@NCNT/Gr-T were synthesized by varying the carbonization temperature ( $T = 700 \text{ °C}, 800 \text{ °C}, 900 \text{ °C}$ ). Taking Ni@NCNT/Gr-800 as an example, firstly, 0.2 g of g- $\text{C}_3\text{N}_4$  was dispersed in 30 mL ethanol by stirring. Then, 0.2 g PVP and 0.2 g  $\text{Ni}(\text{NO}_3)_2 \cdot 6\text{H}_2\text{O}$  were dissolved in the above g- $\text{C}_3\text{N}_4$  suspension solution. After keep stirring for 4 h at room temperature, the mixed suspension solution was kept in an oven overnight to remove the solvent at 80 °C. Next, the dried greenish-

yellow powder was grinded with pestle mortar. Then, the precursor was obtained by carbonizing the grinded powder at 800 °C for 2 h under Ar at the ramping rate of 2 °C min<sup>-1</sup>. Finally, the Ni@NCNT/Gr-800 catalyst was obtained by leaching the precursor in 0.5 M HCl solution at 80 °C for 24 h followed by water washing and drying in an oven. The Ni@NCNT/Gr-700 and Ni@NCNT/Gr-900 catalysts were prepared following the same procedure but with varied carbonization temperatures. Ni@NCNT/Gr-800-48h was prepared using the same route but the acid washing was extended to 48 h.

### 1.2.3 Preparation of Ni@NCNT/Gr-xPVP

A series of Ni@NCNT/Gr-xPVP catalyst ( $x = 1, 2, 3$ ) were synthesized by following the same process as the synthesis of Ni@NCNT/Gr-800 catalyst with different amounts of PVP (0.1 g, 0.2 g, 0.4 g).

### 1.2.4 Preparation of Ni@NCNT/Gr-R catalyst

To further optimize the electrochemical CO<sub>2</sub> reduction performances, a Ni@NCNT/Gr-R catalyst with less Ni content was prepared by following the same process of Ni@NCNT/Gr-800 but with only 0.15 g Ni(NO<sub>3</sub>)<sub>2</sub>·6H<sub>2</sub>O. The final product was defined as Ni@NCNT/Gr-R.

## 2. Materials characterizations

Powder X-ray diffraction patterns (XRD) were acquired at the step length of 0.04° on Bruker D8 equipped with Cu K $\alpha$  radiation ( $\lambda = 1.54 \text{ \AA}$ ). Raman spectra were collected on XploRa (HORIBA) with a laser length of 532 nm. The transmission electron

microscopy (TEM) and high-resolution TEM images equipped with EDX were taken on FEI (Talos F200X G2) at the accelerate voltage of 300 kV. Nitrogen adsorption-desorption isotherm measurements were carried out by QUADRASORB SI (Quantachrome) at 77 K. X-ray photoelectron spectroscopy (XPS) measurement was conducted by Thermo Scientific K-Alpha using monochromatized Al K $\alpha$  ( $h\nu = 1486.7$  eV) as the excitation source. The binding energy was calibrated using the C 1s of graphene oxide nanosheet located at 284.8 eV as the reference. The spectrum deconvolution was conducted using the XPS Peak41 program with Gaussian functions after subtraction of Shirley background.

## **2.1 ICP-MS measurements**

The mass content of Ni in the composite was evaluated by ICP-MS (Aligent 7500 Series). First, 20 mg as-obtained catalyst was dissolved in 150  $\mu$ L HNO<sub>3</sub> and 350  $\mu$ L HCl mixed solution at 70 °C. Then the mixed solution was diluted to a total volume of 10 mL. After that, 100  $\mu$ L destructed solution was then further diluted to 10 mL after adding 150  $\mu$ L HNO<sub>3</sub> and 100  $\mu$ L of 10 ppm Y. A final dilution was made containing 100  $\mu$ L dilution, 100  $\mu$ L of 10 ppm Y (internal standard), 150  $\mu$ L HNO<sub>3</sub> and diluted to 10 mL. 1 ppm standards were made by diluting a 1000 ppm Stock (Alfa Aesar) with HNO<sub>3</sub> and Y.<sup>3</sup>

## **2.2 Electrochemical measurements**

All the electrochemical measurements were performed on an Autolab PGSTAT101. A gas-tight H-cell that was separated by a cation exchange membrane (Nafion 117) was

used as reactor. A platinum electrode (1 cm<sup>2</sup>) was used as the counter electrode. All the potentials reported in this work were converted to vs RHE from vs Ag/AgCl (3 M KCl) according to the following equation.

$$V_{\text{RHE}} = V_{\text{Ag/AgCl}} + 0.21 + 0.0592 \cdot \text{pH} \quad (1)$$

The pH value of the CO<sub>2</sub> saturated 0.5 M KHCO<sub>3</sub> is determined to be 7.2. The linear cyclic voltammetry (LSV) was conducted at the scan rate of 10 mV s<sup>-1</sup> after cyclic voltammetry activation for 20 cycles. The electrochemical active surface area (ECSA) of the obtained catalysts were acquired by measuring their double layer capacitance at various scan rates ( $\nu$ ) in a potential range of 0.1 ~ 0.2 V vs Ag/AgCl. Roughness factor (RF) was calculated according to the ratio of the ECSA on the electrode to the geometric area of the carbon paper electrode based on the equation (2).

$$\text{ECSA} = C_{dl}/C_s \quad (2)$$

where  $C_{dl}$  corresponds to the slope of the double-layer charging current versus the scan rate ( $\nu$ ) plot, we used a specific capacitance ( $C_s$ ) value of 20  $\mu\text{F cm}^{-2}$ . Electrochemical impedance spectroscopy (EIS) measurements were carried out by applying an AC voltage with 10 mV amplitude in a frequency range of 100 kHz ~ 10 mHz. All data are reported in this work without iR compensation.

The liquid product was analyzed by <sup>1</sup>H nuclear magnetic resonance (NMR) with a Bruker Avance III 400 MHz spectrometer. The gas products were determined by gas chromatography (GC, Thermal-Fisher 1310) equipped with a flame ionization detector (FID) and thermal conductivity detector (TCD). Faradaic efficiency (FE) of CO was obtained by equation 3.

$$FE = \frac{Z_i \times V_i \times G \times F \times P_o}{I \times R \times T_o \times 60,000} \quad (3)$$

Where  $Z_i$  indicates the number of electrons required to produce an  $i$  molecule, here,  $i = 2$  for CO and H<sub>2</sub>;  $V_i$  is the volume ratio of product  $i$  in the GC sampling loop;  $G$  suggests the flow rate of CO<sub>2</sub> during the test;  $F$  is the Faradaic constant (96485 C mol<sup>-1</sup>);  $P_o$  represents the atmospheric pressure (1.013 × 10<sup>5</sup> Pa);  $I$  represents the average current in a period ( $t$ ) of electrocatalysis;  $R$  is the ideal gas constant (8.314 J mol<sup>-1</sup> K<sup>-1</sup>);  $T_o$  is the reaction temperature (298 K).

### 3 Theoretical Calculations

Density functional theory (DFT) was performed to calculate the atomic model parameter and investigate the Gibbs free energies of the CO<sub>2</sub> reduction reaction on various N doped NC@Ni models, which was implemented in CASTEP package in the Materials Studio<sup>3, 4</sup>. A vacuum space of 10 Å was applied to avoid the periodic interactions between adjacent layers. Exchange-correlation functions are described by generalized gradient approximation (GGA) with Perdew-Burke-Ernzerhof (PBE) pseudopotentials. A cutoff energy of 400 eV was adopted for these computations. For geometry optimization of the developed models, the following convergent tolerances were set: the maximum force, the changes of energy and the maximum displacement were 0.05 eV Å<sup>-1</sup>, 2 × 10<sup>-5</sup> eV atom<sup>-1</sup>, and 0.002 Å, respectively.

The binding energies ( $E$ ) with H were calculated according to the following equation.<sup>4</sup>

5

$$E = E_{total} - (E_{catalyst} + E_H) \quad (4)$$

where  $E_{total}$ ,  $E_{catalyst}$ , and  $E_H$  denote the calculated total energies of the total bound

systems, H, and the developed models (G, Ni, Pyrrolic N-Gr, graphitic N-Gr/Ni, pyridinic N-Gr/Ni and Pyrrolic N-Gr/Ni), respectively.

## Supplementary Figures

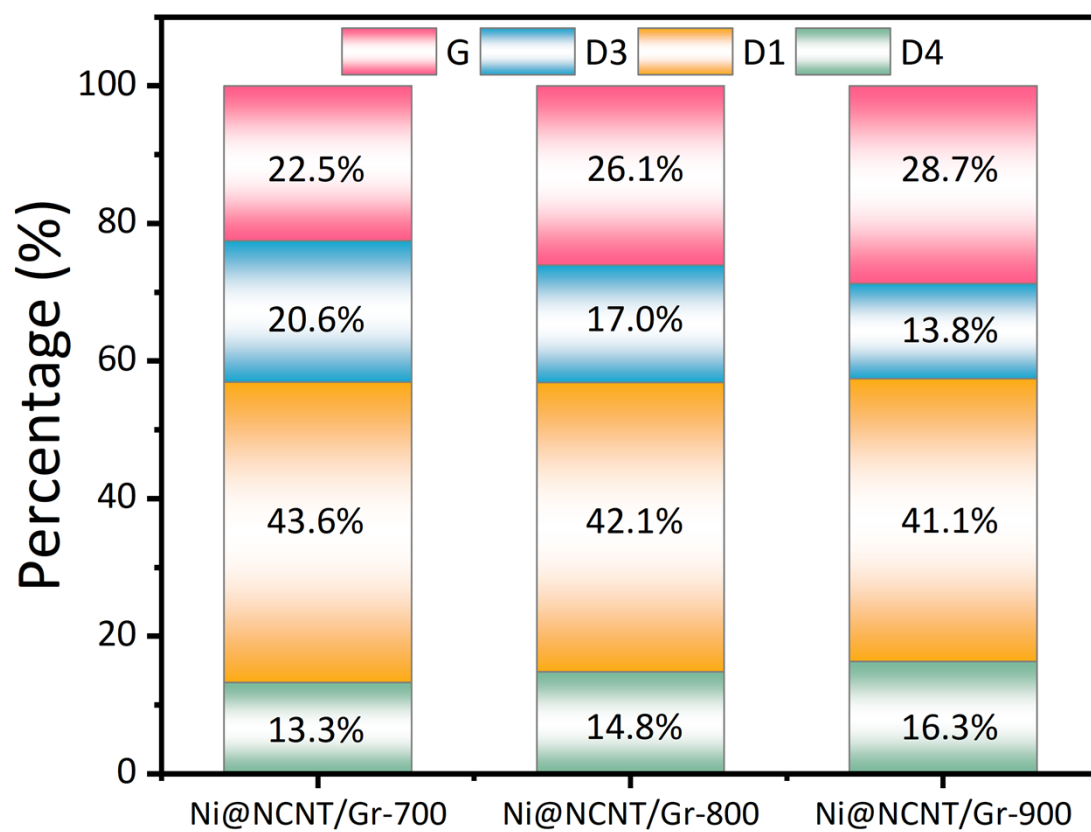


**Figure S1.** Percentage of various deconvoluted D and G bands from Raman spectra.

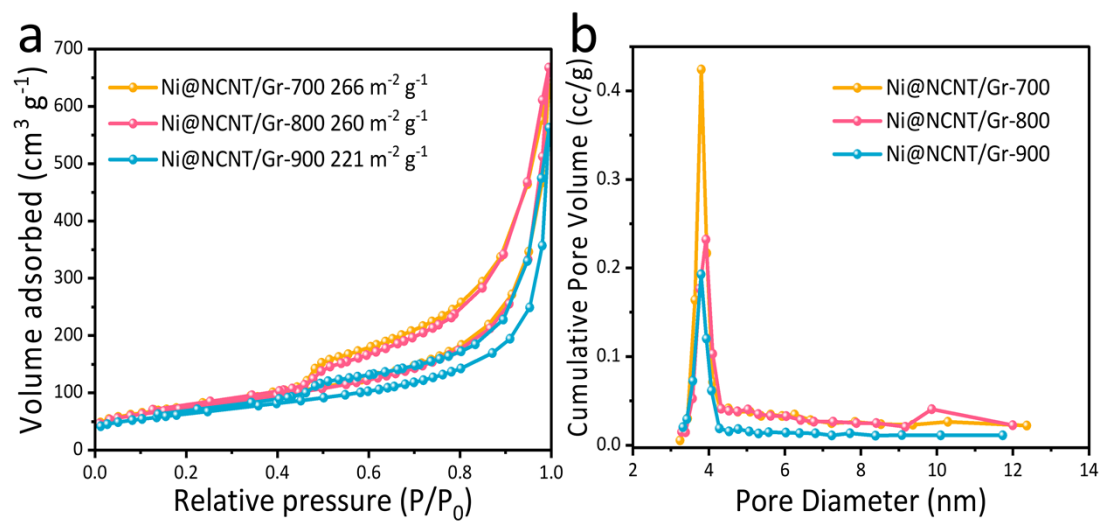


**Figure S2.** a) N<sub>2</sub> adsorption-desorption isotherms, and b) Porosity distribution of the Ni@NCNT/Gr-T (T = 700, 800, 900 °C) catalysts.

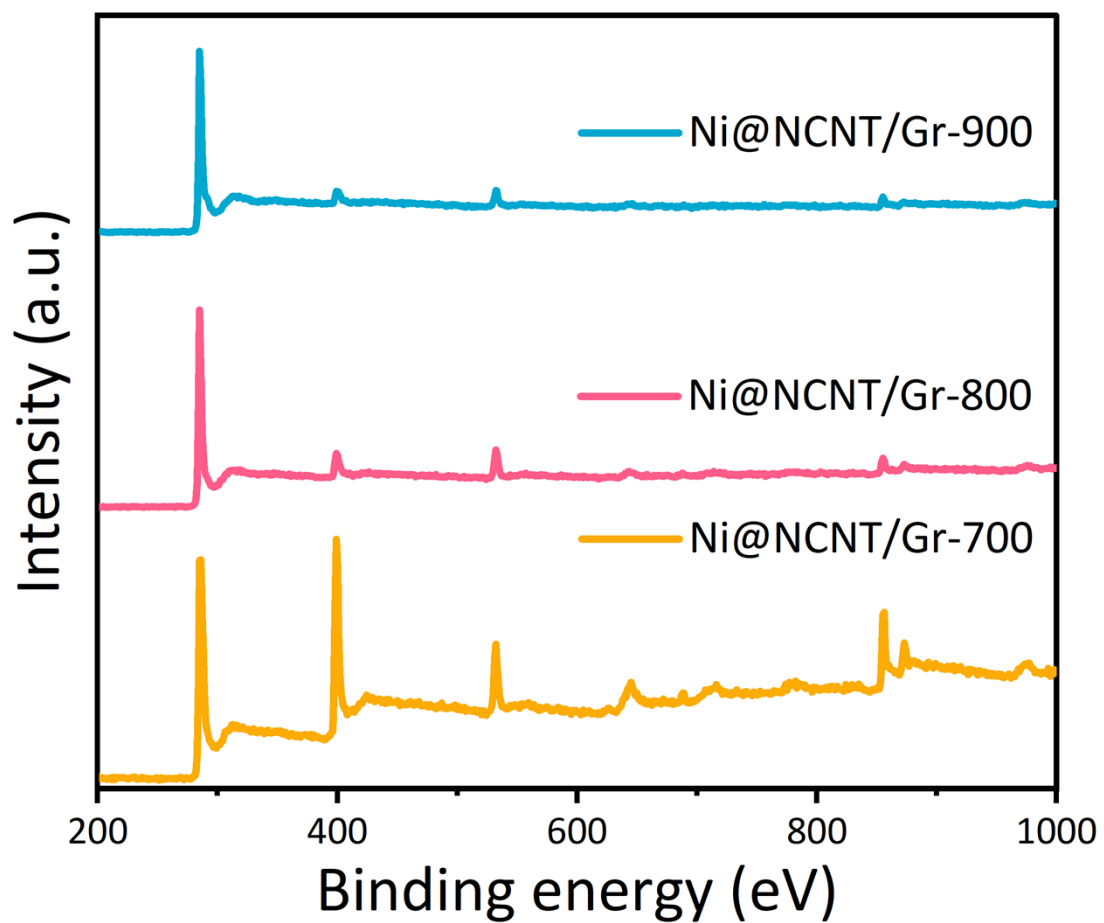


**Figure S3.** XPS survey spectra of Ni@NCNT/Gr-T (T = 700, 800, 900 °C) catalysts obtained at various temperatures.

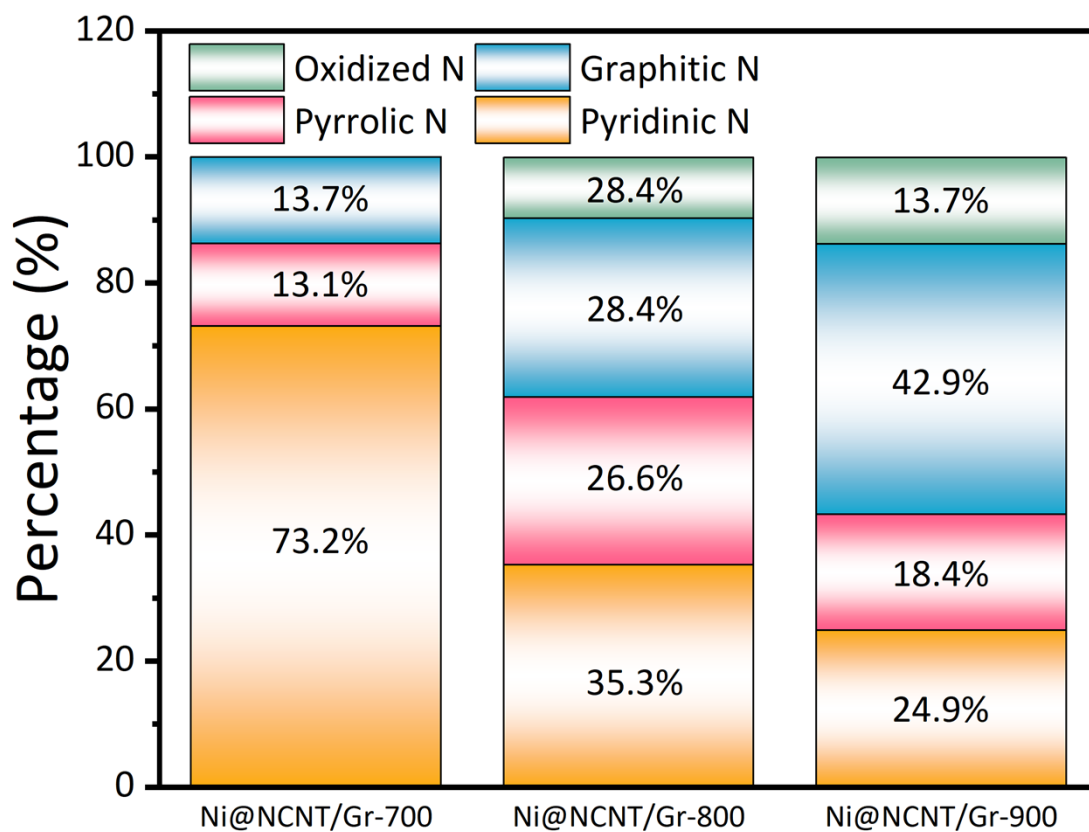


**Figure S4.** Percentages of pyridinic N, pyrrolic N, graphitic N, and oxidized N of the obtained Ni@NCNT/Gr-T (T = 700, 800, 900 °C) **catalysts** (based on XPS results).

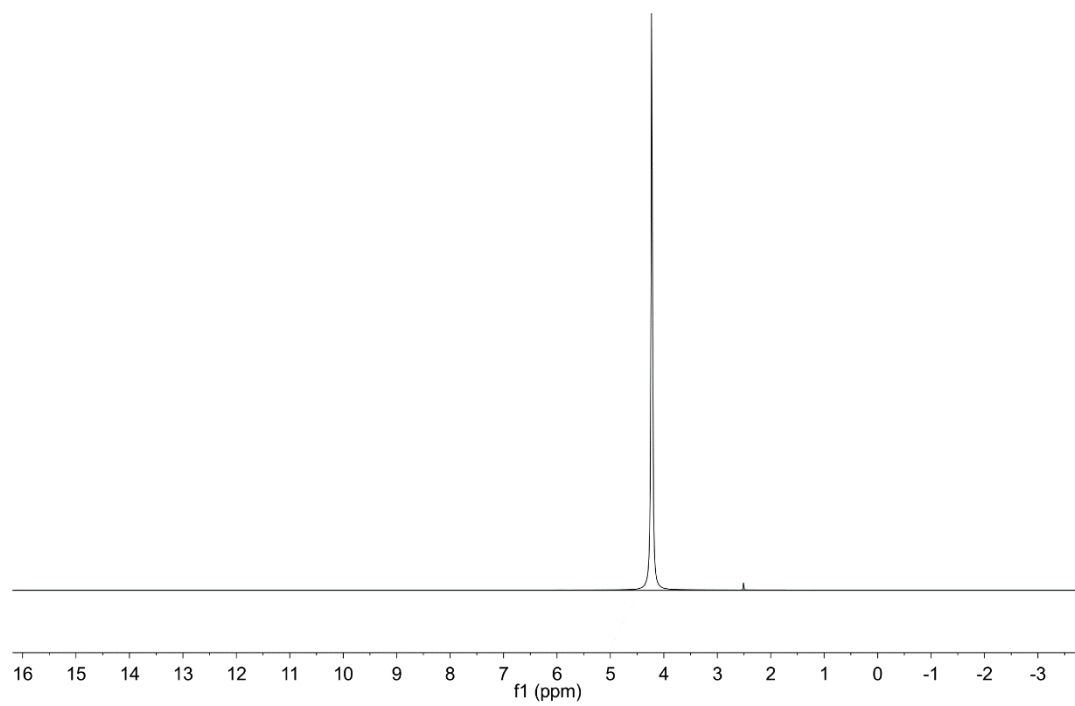


**Figure S5.**  $^1\text{H}$  NMR spectra of the 0.5 M  $\text{KHCO}_3$  electrolyte after electrolysis for 24 h.

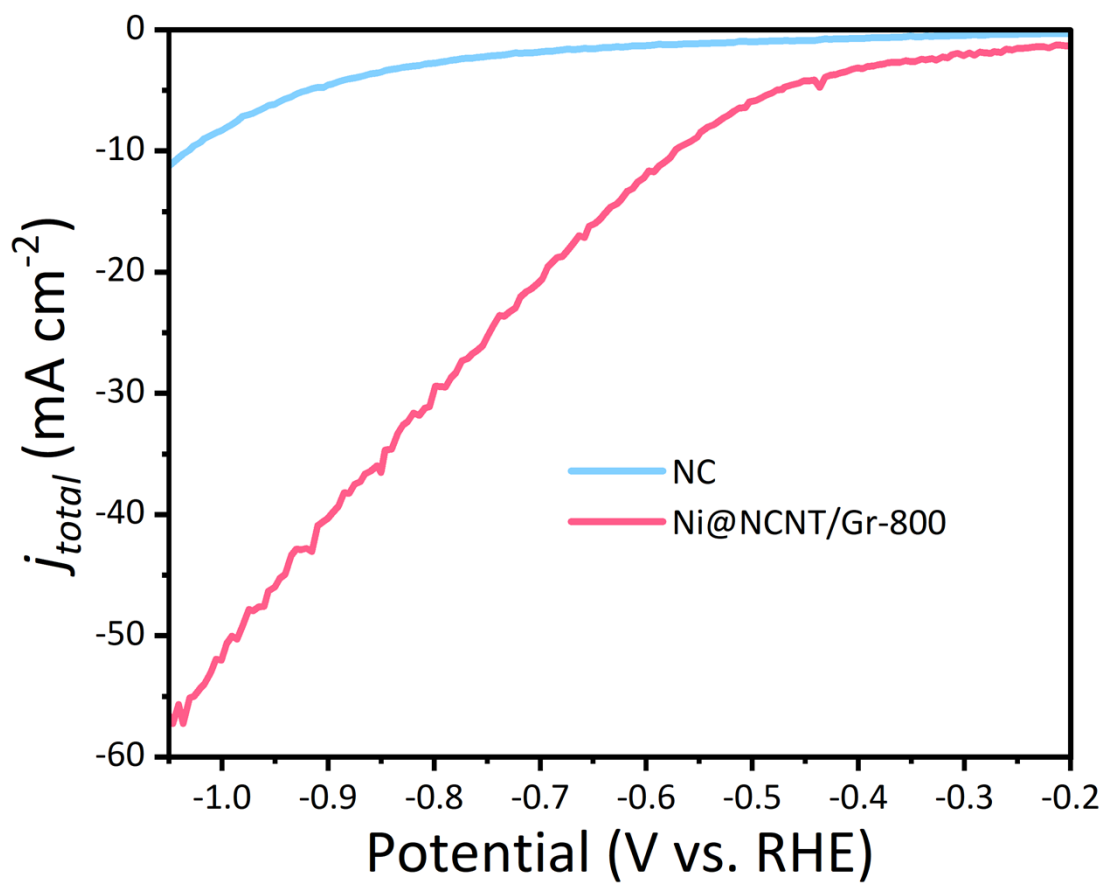


**Figure S6.** LSV curves of Ni@NCNT/Gr-800 and NC at the scan rate of  $10 \text{ mV s}^{-1}$ .

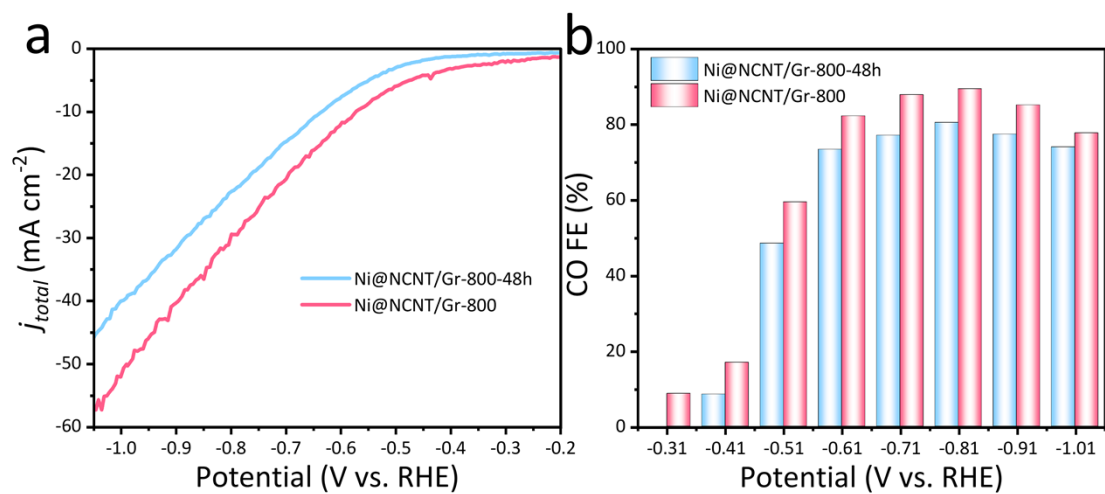


**Figure S7.** a) LSV curves of Ni@NCNT/Gr-800 and Ni@NCNT/Gr-800-48h at the scan rate of  $10 \text{ mV s}^{-1}$ ; b) CO FE of Ni@NCNT/Gr-800 and Ni@NCNT/Gr-800-48h.

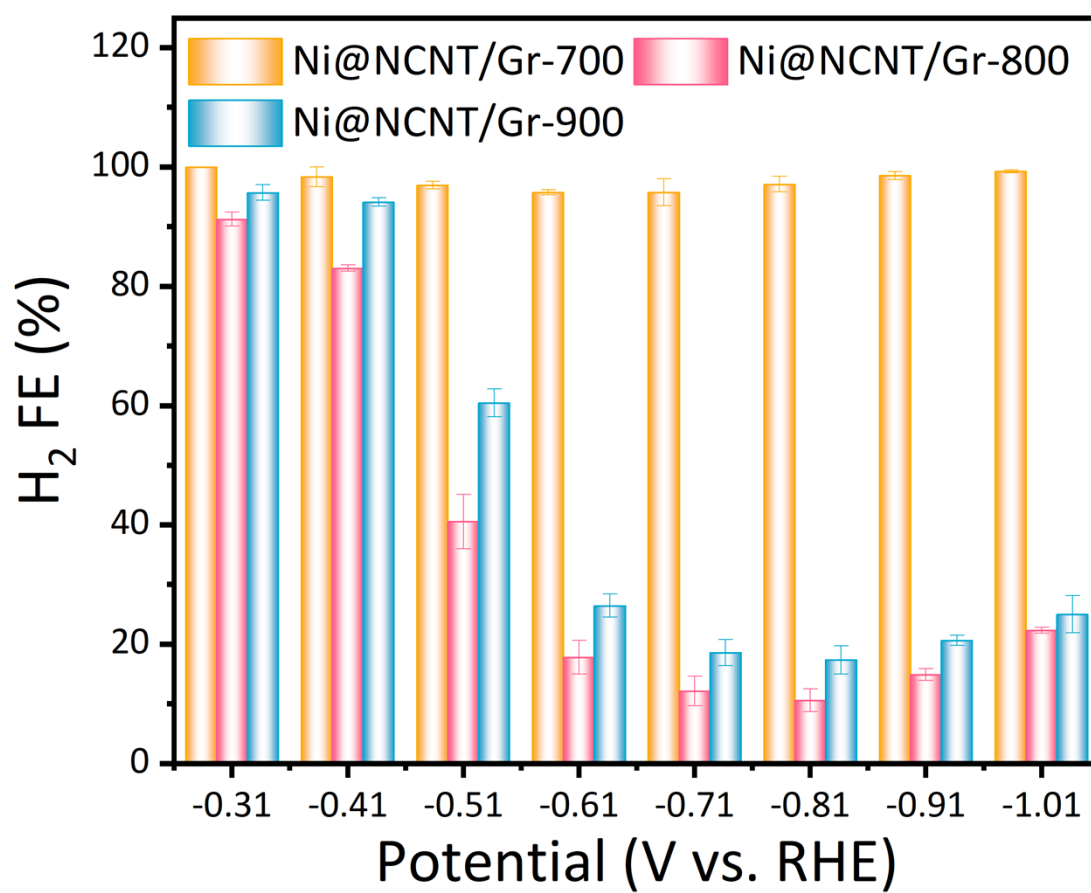


**Figure S8.** H<sub>2</sub> FE of the as-prepared catalysts Ni@NCNT/Gr-T (T = 700, 800, 900 °C) obtained at various temperatures.

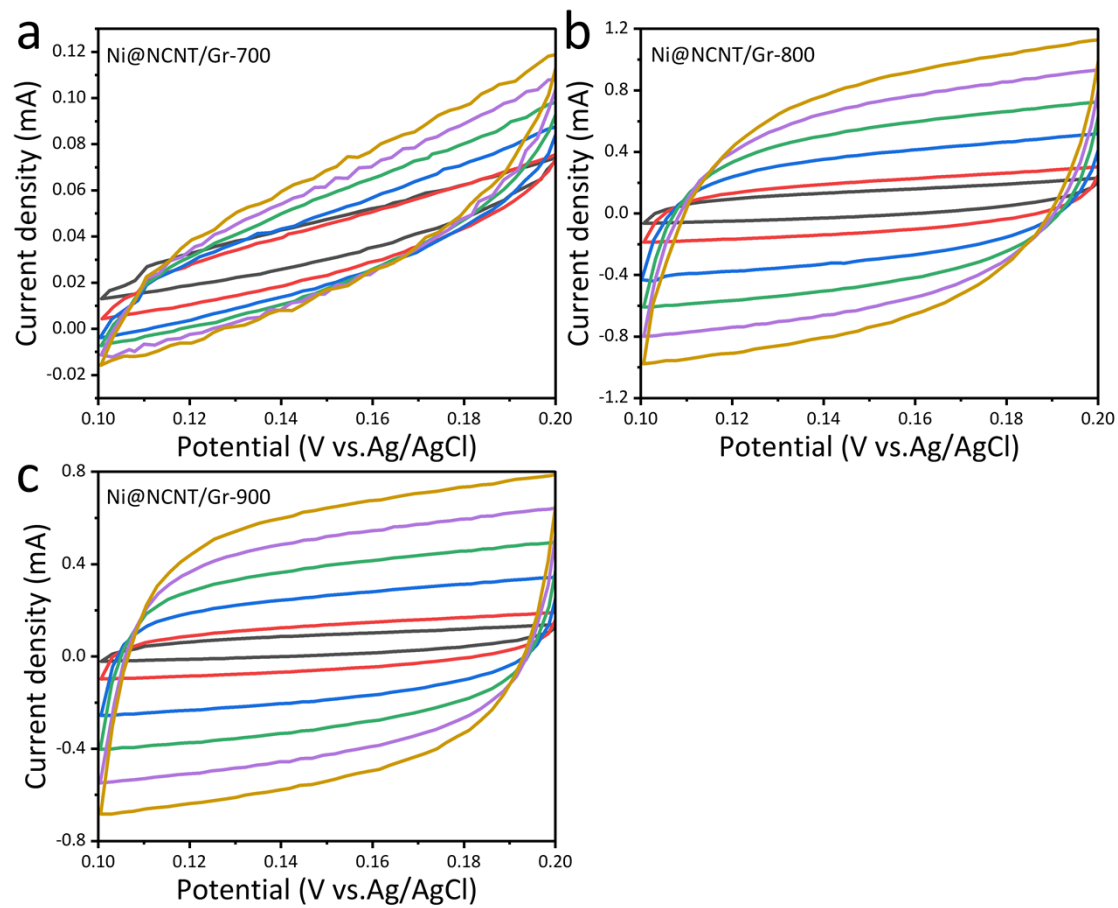


**Figure S9.** Cyclic voltammetry measurements for Ni@NCNT/Gr-T (T = 700, 800, 900 °C) at scan rates varying from 10 to 100 mV s<sup>-1</sup>.

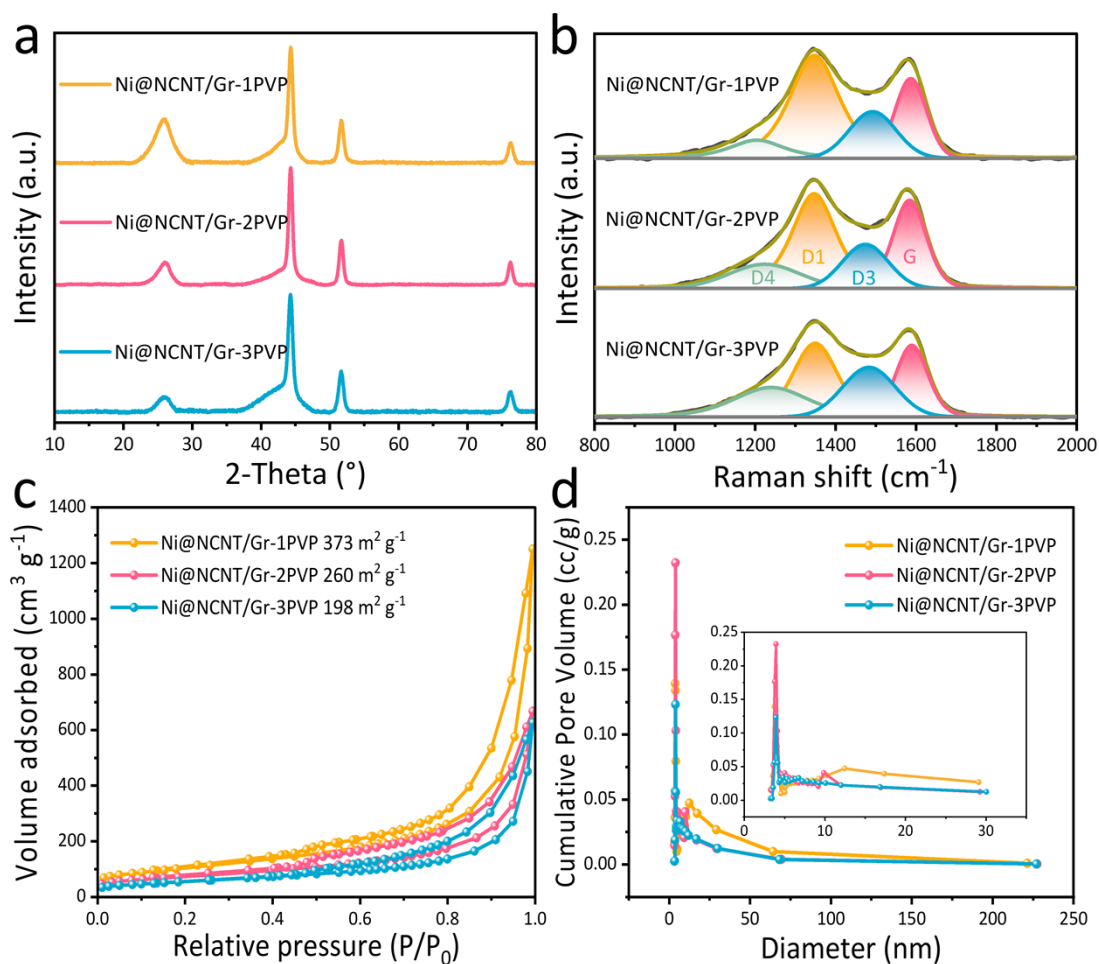


**Figure S10.** a) XRD pattern, b) Raman spectra, c) N<sub>2</sub> adsorption-desorption isotherms, and d) Porosity distribution of the Ni@NCNT/Gr-*x*PVP (*x* = 1, 2, 3) catalysts obtained with different amounts of PVP (0.1 g, 0.2 g, 0.4 g).

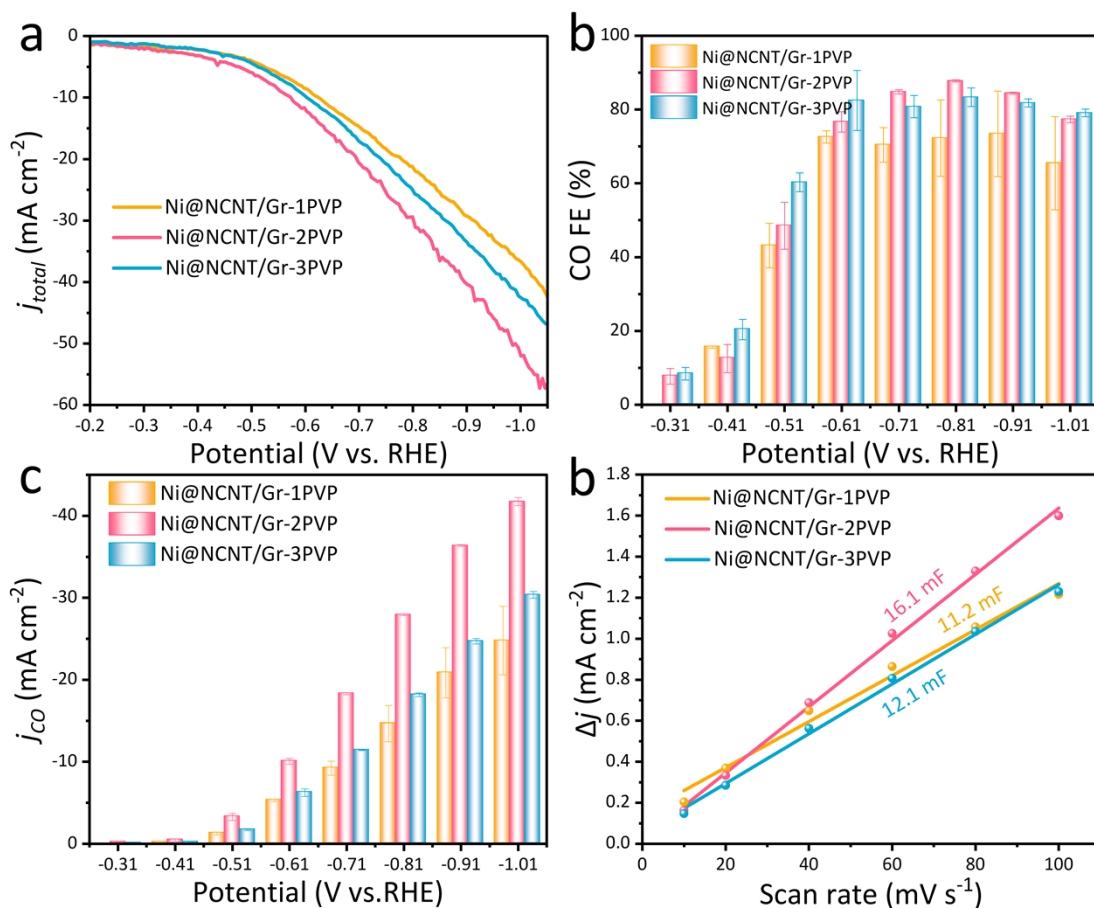


**Figure S11.** ECO<sub>2</sub>RR performances of the Ni@NCNT/Gr-*x*PVP (*x* = 1, 2, 3) catalysts. a) LSV curves of the Ni@NCNT/Gr-*x*PVP catalysts in CO<sub>2</sub> saturated 0.5 M KHCO<sub>3</sub> at a scan rate of 10 mV s<sup>-1</sup>, b) and c) CO FEs and  $j_{CO}$  at various potentials (Vs. RHE), d) Charging current density differences plotted against scan rates, roughness factor (RF) of Ni@NCNT/Gr-1PVP, Ni@NCNT/Gr-2PVP, Ni@NCNT/Gr-3PVP electrodes are 560, 805, and 605, respectively.

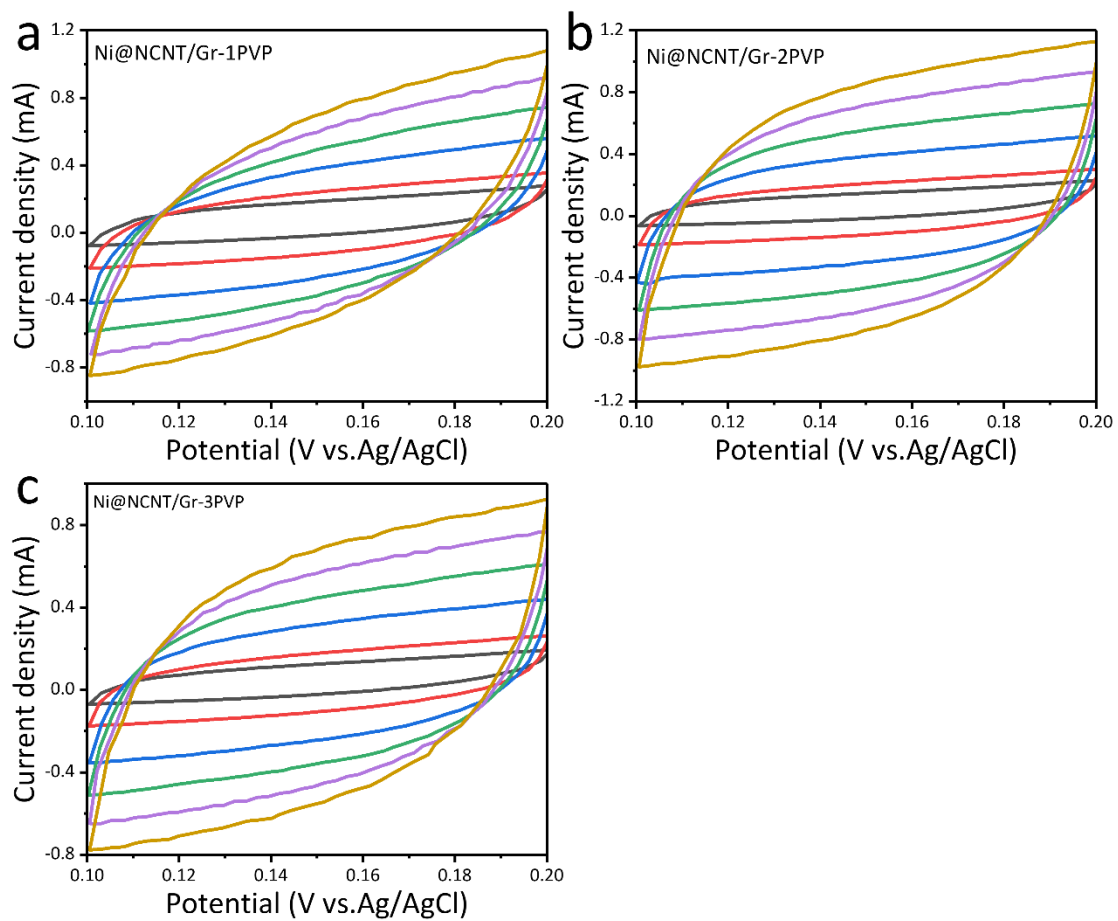


**Figure S12.** Cyclic voltammetry measurements for Ni@NCNT/Gr-xPVP (x = 1, 2, 3) at scan rates varying from 10 to 100 mV s<sup>-1</sup>.

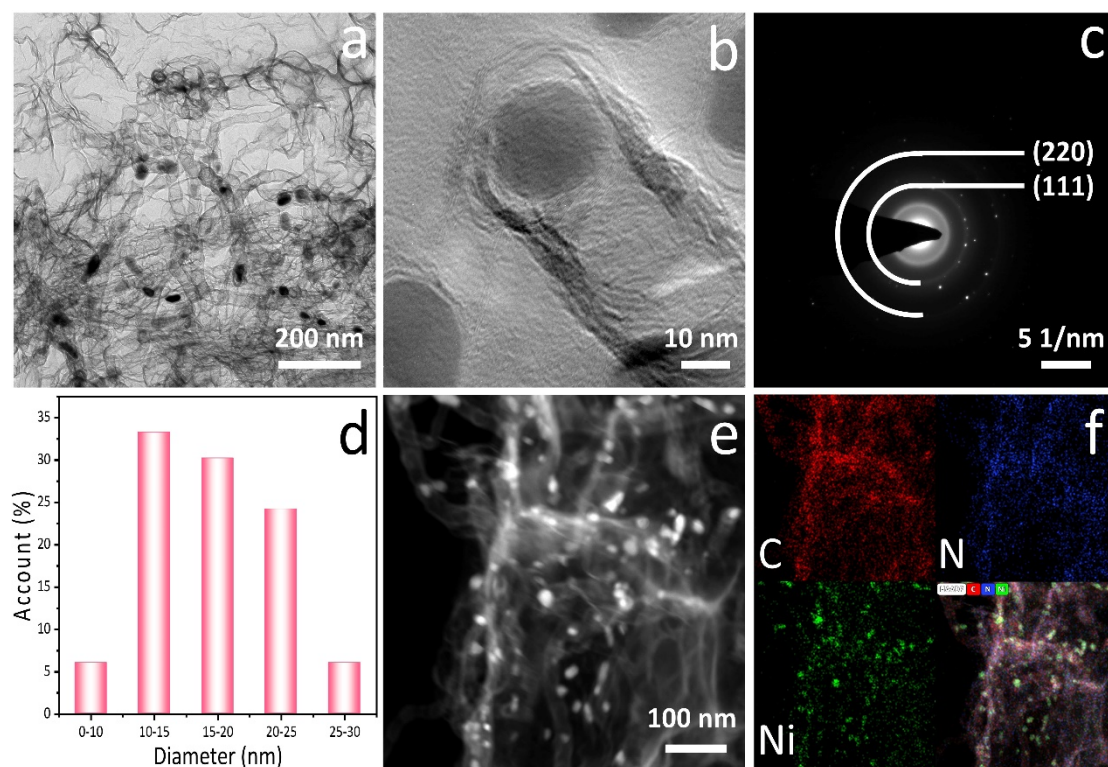


**Figure S13.** a) and b) TEM and HRTEM image, c) SAED pattern, d) Particle size distribution, e) and f) elemental mapping of the as-prepared Ni@NCNT/Gr-R catalyst.

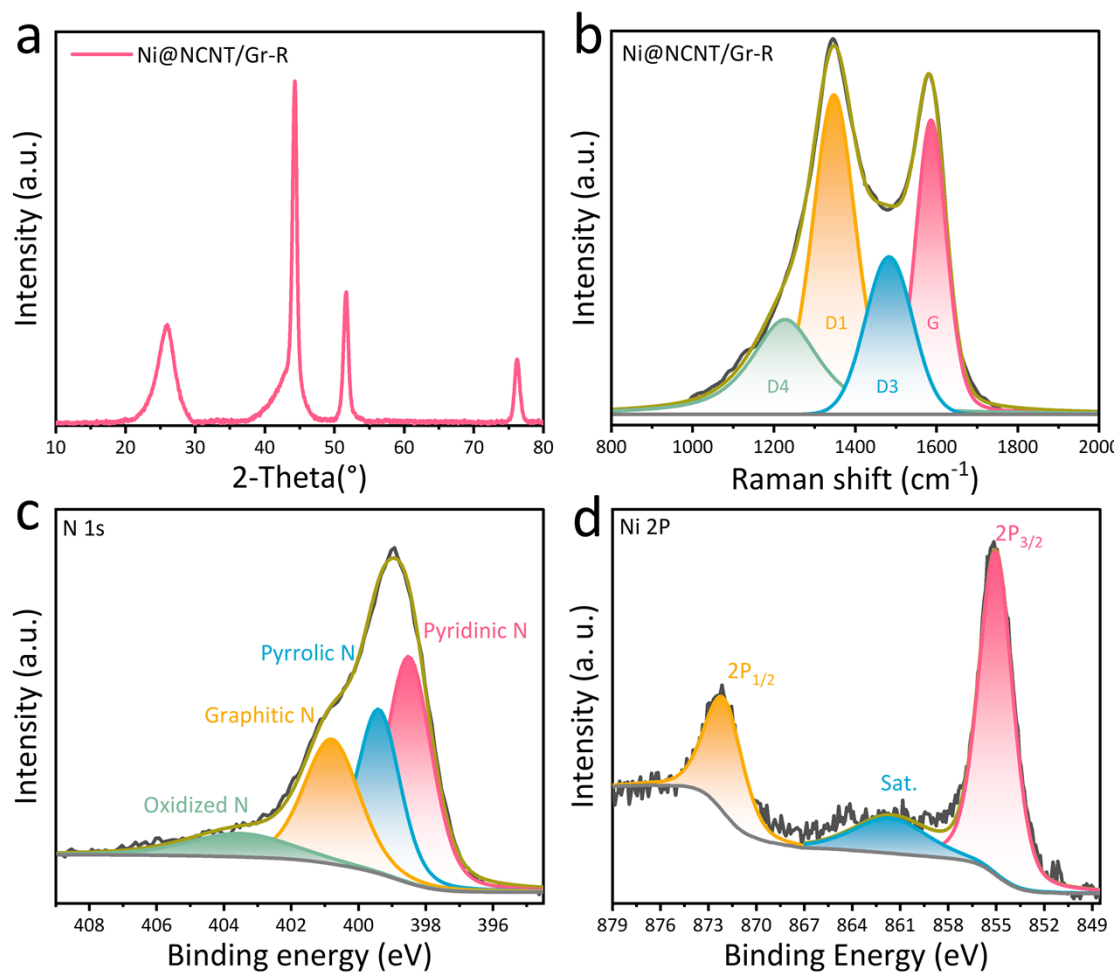


**Figure S14.** a) XRD pattern, b) Raman spectra, c) High resolution N 1s XPS spectra, d) High resolution Ni 2p XPS spectra of the Ni@NCNT/Gr-R catalyst.

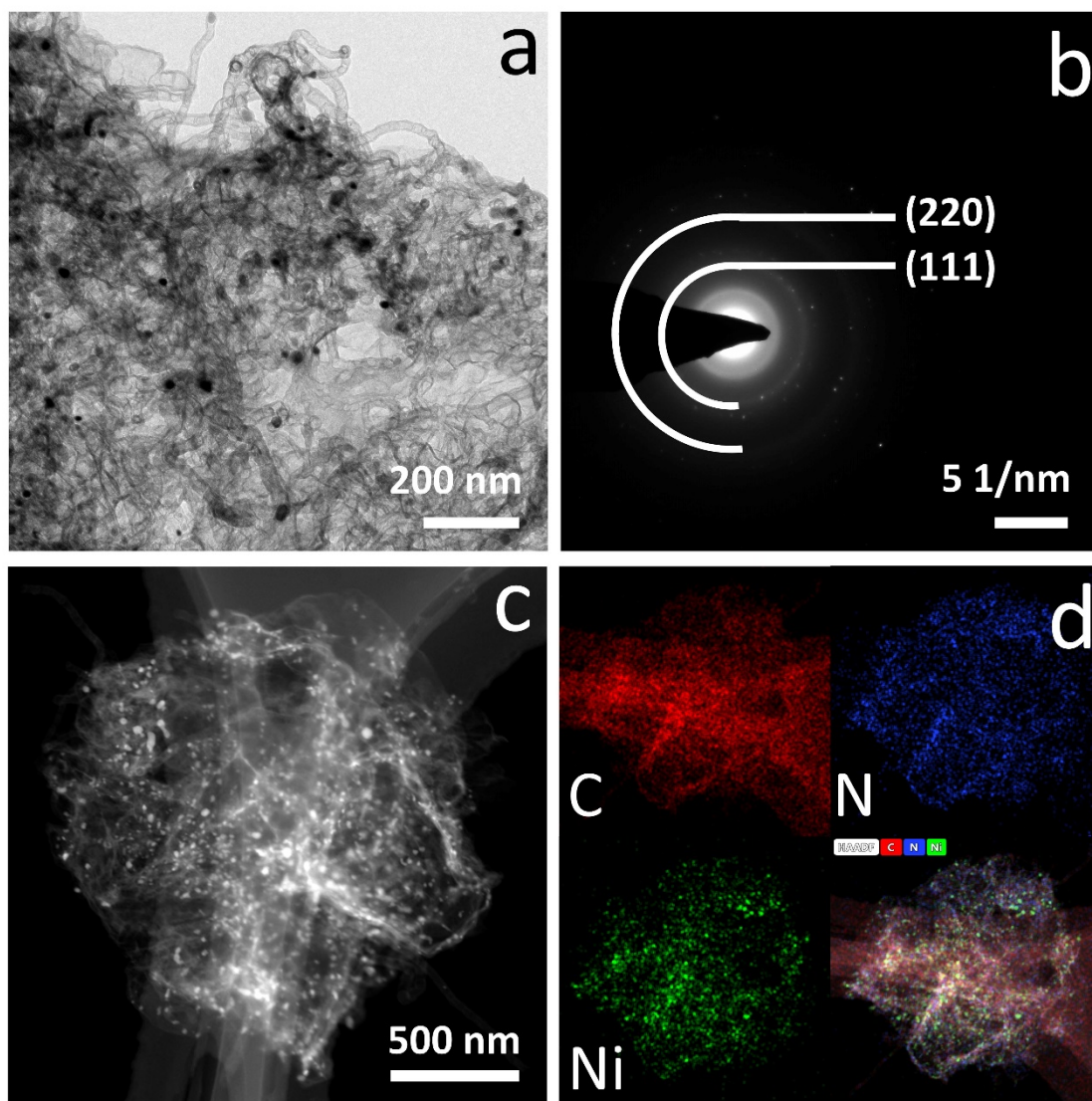


**Figure S15.** a) TEM image, b) SAED pattern, c) HAADF image and d) Elemental mapping of Ni@NCNT/Gr-R after electrolysis at  $-0.71$  V for 24 h.

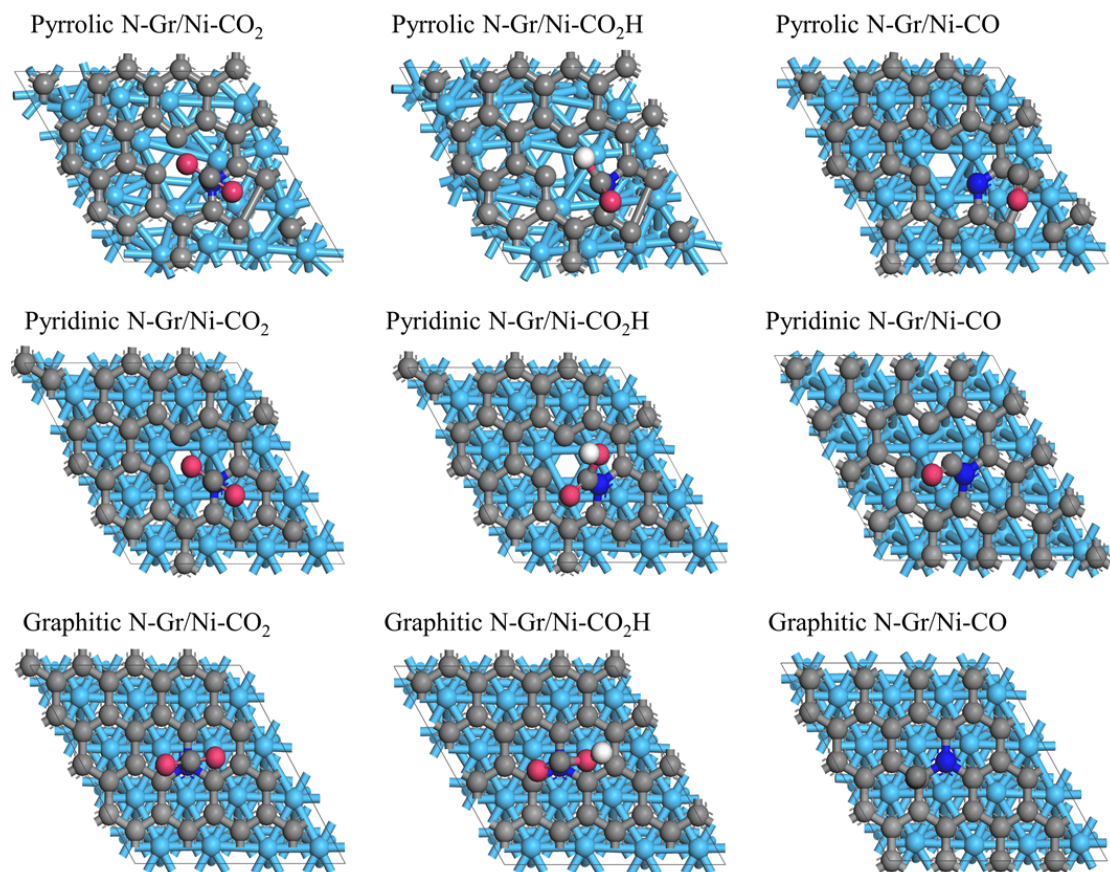


**Figure S16.** Optimized calculation models of pyrrolic N-Gr/Ni, pyridinic N-Gr/Ni, and Graphitic N-Gr/Ni with different absorbates.

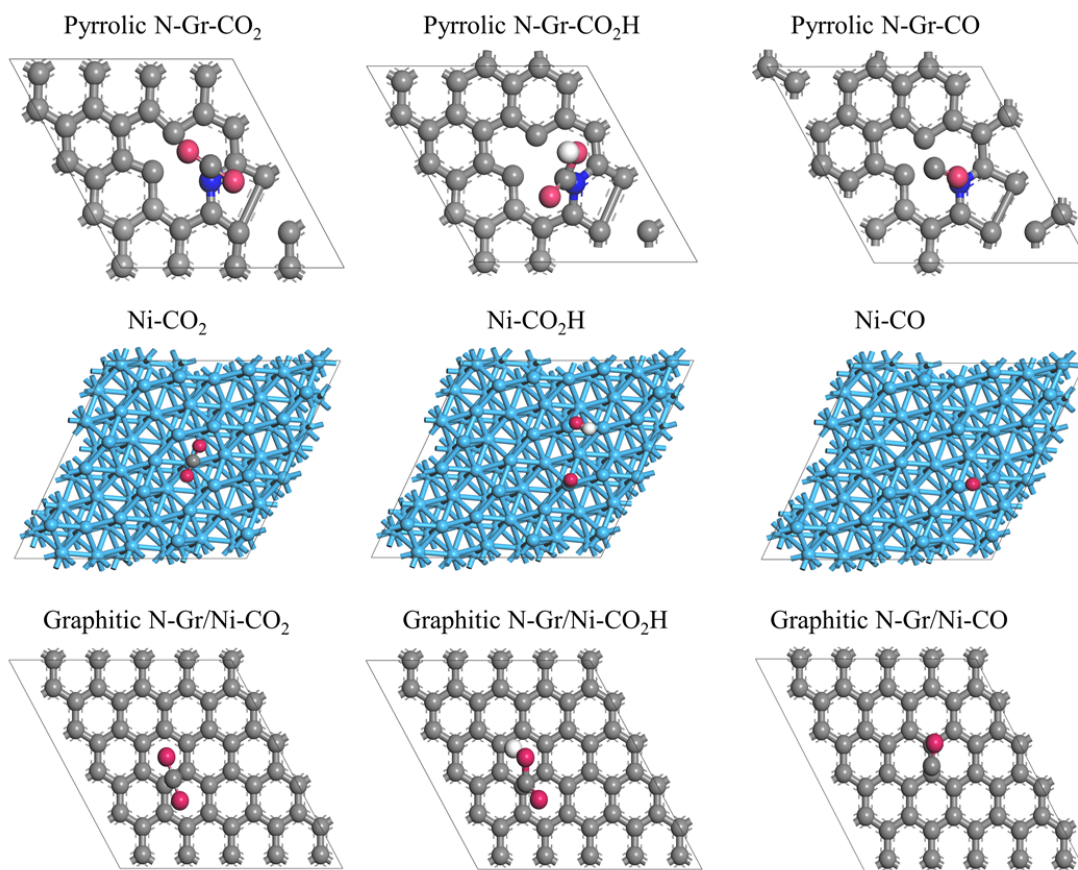


**Figure S17.** Optimized calculation models of pyrrolic N-Gr, Ni (111), and Graphitic N-Gr with different absorbates.

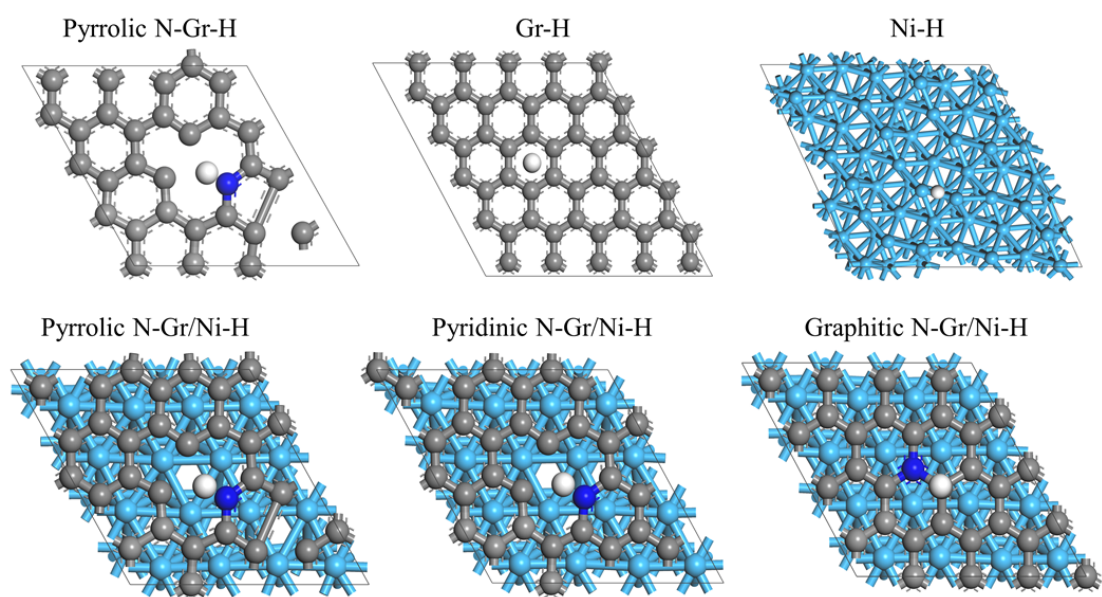


**Figure S18.** Optimized calculation models with absorbed  $^*H$ .

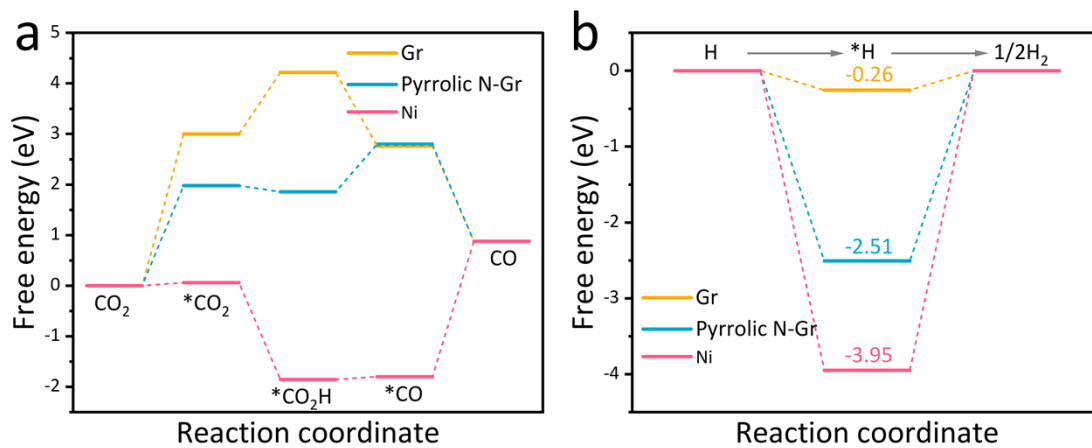


**Figure S19.** a) The calculated free energy diagrams for ECO2RR to CO on graphene, pyrrolic N-doped graphene, and bare Ni. b) The calculated free energy diagrams for HER to  $\text{H}_2$  on graphene, pyrrolic N-doped graphene, and bare Ni.

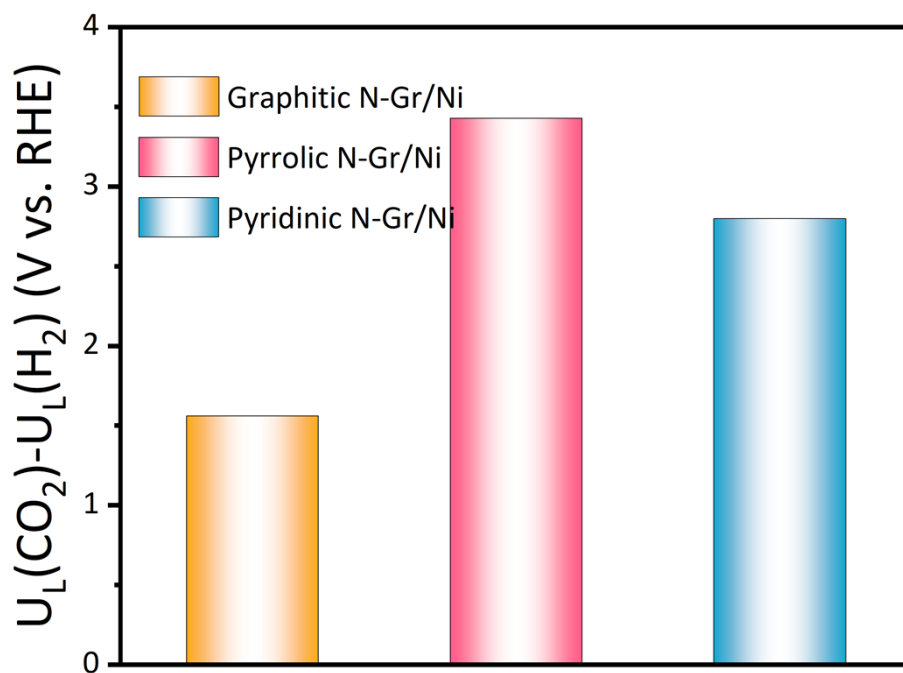


**Figure S20.** Limiting potential difference for ECO2RR and HER on Pyrrolic N-Gr/Ni, Pyridinic N-Gr/Ni, and Graphitic N-Gr/Ni.

**Table S1.** Comparison of ECO2RR performances with recently reported advanced catalysts in H-type cell.

Catalyst	Potential (V vs. RHE)	$FE_{CO}$ (%)	$j_{CO}$ (mA cm <sup>-2</sup> )	Tafel (mV dec <sup>-1</sup> )	potential range over 90% (V)	Ref.
<b>Ni@NCNT/Gr-R</b>	<b>-0.71</b>	<b>91.5</b>	<b>16.9</b>	<b>147.4</b>	<b>-0.71 ~ -0.91</b>	<b>This work</b>
	<b>-0.91</b>	<b>92.1</b>	<b>37.4</b>			
<b>Ni@NCNT/Gr-800</b>	<b>-0.81</b>	<b>87.8</b>	<b>27.9</b>	<b>147.7</b>	/	
NiNG	-0.80	97	40.3@-0.9 V	61.2	-0.7 ~ -0.80	6
Ni(NC)-1	-0.75	> 99	< 17	199	-0.65 ~ -0.90	7
FeNPs-NC	-0.60	93	7.1	122	-0.6 ~ -0.80	8
Fe-N/O-C (MZ)	-0.57	96	5.6	/	-0.52 ~ -0.62	9
Ni@N-C	-0.77	90	< 9.4	128.2	-0.77	10
Ni@N-C	-0.80	90	21.8@-1.0 V	95.09	-0.80	11
Fe <sub>2</sub> NPC	-0.60	96	2.9	60	-0.6 ~ -0.7	12
NiSA-NGA-900	-0.80	90.2	< 7	125	-0.80	13
Ni-CNC-1000	-0.80	96.6	< 10	124.6	-0.7 ~ -0.95	14
Ni SAs	-0.80	97	< 8	/	-0.7 ~ -1.0	15
I-Ni SA/NHCRs	-0.80	94.91	15.35	155±5	-0.7 ~ -0.9	16
FeN/Fe <sub>3</sub> N	-0.40	98	21@-0.9 V	/	-0.5 ~ -0.9	17
Ni-N-C	-0.65	97	< 10	/	-0.5 ~ -0.9	18
H-NiFe/NG	-0.80	94	< 8	83	-0.8 ~ -1.0	19
Ni/N-CNTs-10	-0.65	98	5.3	/	-0.65 ~ -0.75	20
Ni <sub>4</sub> N/Ni <sub>3</sub> ZnCo <sub>0.7</sub> -0.2	-0.80	92.3	14.6	123	-0.75 ~ -0.80	21
FeN <sub>4</sub> -O	-0.50	95	< 5	29	-0.45 ~ -0.55	22
as-PorCo	-0.60	93	< 8	161	-0.5 ~ -0.70	23
Cu-In-NC	-0.70	96	5.8@-0.8 V	121.6	-0.7 ~ -0.80	24
NiSA-N-CNTs	-0.70	91.3	23.5	/	-0.70	25
CNT-SMX-250	-0.76	91.5	14	/	-0.7 ~ -0.90	26
Fe-N-PC	-0.49	~90	11.44	/	-0.49	27
Ni <sub>SA</sub> -N <sub>x</sub> -C	-0.80	~98	~5	208	-0.8	28
Ni-N-C	-0.67	94	-3.9	119	-0.67 ~ -0.87	29

## References

- (1) Cao, S.; Low, J.; Yu, J.; Jaroniec, M. Polymeric photocatalysts based on graphitic carbon nitride. *Adv. Mater.* **2015**, *27* (13), 2150-2176.
- (2) Maeda, K.; Wang, X.; Nishihara, Y.; Lu, D.; Antonietti, M.; Domen, K. Photocatalytic Activities of Graphitic Carbon Nitride Powder for Water Reduction and Oxidation under Visible Light. *J. Phys. Chem. C* **2009**, *113* (12), 4940-4947.
- (3) Wang, Q.; Nakabayashi, M.; Hisatomi, T.; Sun, S.; Akiyama, S.; Wang, Z.; Pan, Z.; Xiao, X.; Watanabe, T.; Yamada, T.; et al. Oxysulfide photocatalyst for visible-light-driven overall water splitting. *Nat. Mater.* **2019**, *18* (8), 827-832.
- (4) Liu, C.; Han, M.; Cao, Y.; Chen, L.; Ren, W.; Zhou, G.; Chen, A.; Sun, J. Unlocking the dissolution mechanism of phosphorus anode for lithium-ion batteries. *Energy Storage Mater.* **2021**, *37*, 417-423.
- (5) Liang, X.; Rangom, Y.; Kwok, C. Y.; Pang, Q.; Nazar, L. F. Interwoven MXene Nanosheet/Carbon-Nanotube Composites as Li-S Cathode Hosts. *Adv. Mater.* **2017**, *29* (3), 1603040.
- (6) Jia, C.; Tan, X.; Zhao, Y.; Ren, W.; Li, Y.; Su, Z.; Smith, S. C.; Zhao, C. Sulfur-Dopant-Promoted Electroreduction of CO<sub>2</sub> over Coordinatively Unsaturated Ni-N<sub>2</sub> Moieties. *Angew. Chem.-Int. Ed.* **2021**, *60* (43), 23342-23348.
- (7) Wen, C. F.; Mao, F.; Liu, Y.; Zhang, X. Y.; Fu, H. Q.; Zheng, L. R.; Liu, P. F.; Yang, H. G. Nitrogen-Stabilized Low-Valent Ni Motifs for Efficient CO<sub>2</sub> Electro catalysis. *ACS Catal.* **2019**, *10* (2), 1086-1093.
- (8) Fan, Q.; Bao, G.; Chen, X.; Meng, Y.; Zhang, S.; Ma, X. Iron Nanoparticles Tuned to Catalyze CO<sub>2</sub> Electroreduction in Acidic Solutions through Chemical Microenvironment Engineering. *ACS Catal.* **2022**, *12* (13), 7517-7523.
- (9) Wang, X.; Pan, Y.; Ning, H.; Wang, H.; Guo, D.; Wang, W.; Yang, Z.; Zhao, Q.; Zhang, B.; Zheng, L.; et al. Hierarchically micro- and meso-porous Fe-N<sub>4</sub>O-doped carbon as robust electrocatalyst for CO<sub>2</sub> reduction. *Appl. Catal. B* **2020**, *266*, 118630.
- (10) Meng, J.; Miao, Z.; Zhang, J.; Wang, Z.; Zhang, R.; Xu, L.; Diao, L.; Zhou, J.; Zhuo, S. One-step synthesis of N-doped carbon nanotubes-encapsulated Ni nanoparticles for efficient electrochemical CO<sub>2</sub> reduction to CO. *J. Alloys. Compd.* **2023**, *939*, 168798.
- (11) Wang, F.; Wang, G.; Deng, P.; Chen, Y.; Li, J.; Wu, D.; Wang, Z.; Wang, C.; Hua, Y.; Tian, X. Ultrathin Nitrogen-Doped Carbon Encapsulated Ni Nanoparticles for Highly Efficient Electrochemical CO<sub>2</sub> Reduction and Aqueous Zn-CO<sub>2</sub> Batteries. *Small* **2023**, *19* (25), e2301128.
- (12) Zhao, X.; Zhao, K.; Liu, Y.; Su, Y.; Chen, S.; Yu, H.; Quan, X. Highly Efficient Electrochemical CO<sub>2</sub> Reduction on a Precise Homonuclear Diatomic Fe-Fe Catalyst. *ACS Catal.* **2022**, *12* (18), 11412-11420.
- (13) Mou, K.; Chen, Z.; Zhang, X.; Jiao, M.; Zhang, X.; Ge, X.; Zhang, W.; Liu, L. Highly Efficient Electroreduction of CO<sub>2</sub> on Nickel Single-Atom Catalysts: Atom Trapping and Nitrogen Anchoring. *Small* **2019**, *15* (49), e1903668.
- (14) Cao, X.; Zhao, L.; Wulan, B.; Tan, D.; Chen, Q.; Ma, J.; Zhang, J. Atomic Bridging Structure of Nickel-Nitrogen-Carbon for Highly Efficient Electrocatalytic Reduction of CO<sub>2</sub>. *Angew. Chem.-Int. Ed.* **2022**, *61* (6), e202113918.
- (15) Li, Z.; He, D.; Yan, X.; Dai, S.; Younan, S.; Ke, Z.; Pan, X.; Xiao, X.; Wu, H.; Gu, J. Size-Dependent Nickel-Based Electrocatalysts for Selective CO<sub>2</sub> Reduction. *Angew. Chem.-Int. Ed.* **2020**, *59* (42), 18572-18577.
- (16) Gong, S.; Yang, S.; Wang, W.; Lu, R.; Wang, H.; Han, X.; Wang, G.; Xie, J.; Rao, D.; Wu, C.; et

al. Promoting CO<sub>2</sub> Dynamic Activation via Micro-Engineering Technology for Enhancing Electrochemical CO<sub>2</sub> Reduction. *Small* **2023**, *19* (26), e2207808.

(17) Yin, J.; Jin, J.; Yin, Z.; Zhu, L.; Du, X.; Peng, Y.; Xi, P.; Yan, C. H.; Sun, S. The built-in electric field across FeN/Fe<sub>3</sub>N interface for efficient electrochemical reduction of CO<sub>2</sub> to CO. *Nat. Commun.* **2023**, *14* (1), 1724.

(18) Wang, J.; Huang, Y.-C.; Wang, Y.; Deng, H.; Shi, Y.; Wei, D.; Li, M.; Dong, C.-L.; Jin, H.; Mao, S. S.; et al. Atomically Dispersed Metal–Nitrogen–Carbon Catalysts with d-Orbital Electronic Configuration-Dependent Selectivity for Electrochemical CO<sub>2</sub>-to-CO Reduction. *ACS Catal.* **2023**, *13* (4), 2374-2385.

(19) He, Q.; Zhang, Y.; Li, H.; Yang, Y.; Chen, S.; Yan, W.; Dong, J.; Zhang, X. M.; Fan, X. Engineering Steam Induced Surface Oxygen Vacancy onto Ni-Fe Bimetallic Nanocomposite for CO<sub>2</sub> Electroreduction. *Small* **2022**, *18* (15), e2108034.

(20) Wu, S.; Yi, F.; Ping, D.; Huang, S.; Zhang, Y.; Han, L.; Wang, S.; Wang, H.; Yang, X.; Guo, D.; et al. Constructing single-atomic nickel sites in carbon nanotubes for efficient CO<sub>2</sub> electroreduction. *Carbon* **2022**, *196*, 1-9.

(21) Wang, J.; Li, Z.; Zhu, Z.; Jiang, J.; Li, Y.; Chen, J.; Niu, X.; Chen, J. S.; Wu, R. Tailoring the interactions of heterostructured Ni<sub>4</sub>N/Ni<sub>3</sub>ZnC<sub>0.7</sub> for efficient CO<sub>2</sub> electroreduction. *J. Energy Chem.* **2022**, *75*, 1-7.

(22) Zhang, T.; Han, X.; Liu, H.; Biset-Peiró, M.; Li, J.; Zhang, X.; Tang, P.; Yang, B.; Zheng, L.; Morante, J. R.; et al. Site-Specific Axial Oxygen Coordinated FeN<sub>4</sub> Active Sites for Highly Selective Electroreduction of Carbon Dioxide. *Adv. Funct. Mater.* **2022**, *32* (18), 2111446.

(23) Bao, W.; Huang, S.; Tranca, D.; Feng, B.; Qiu, F.; Rodriguez-Hernandez, F.; Ke, C.; Han, S.; Zhuang, X. Molecular Engineering of Co<sup>II</sup> Porphyrins with Asymmetric Architecture for Improved Electrochemical CO<sub>2</sub> Reduction. *ChemSusChem* **2022**, *15* (8), e202200090.

(24) Hu, C.; Wang, Y.; Chen, J.; Wang, H. F.; Shen, K.; Tang, K.; Chen, L.; Li, Y. Main-Group Metal Single-Atomic Regulators in Dual-Metal Catalysts for Enhanced Electrochemical CO<sub>2</sub> Reduction. *Small* **2022**, *18* (22), e2201391.

(25) Cheng, Y.; Zhao, S.; Johannessen, B.; Veder, J. P.; Saunders, M.; Rowles, M. R.; Cheng, M.; Liu, C.; Chisholm, M. F.; De Marco, R.; et al. Atomically Dispersed Transition Metals on Carbon Nanotubes with Ultrahigh Loading for Selective Electrochemical Carbon Dioxide Reduction. *Adv. Mater.* **2018**, *30* (13), e1706287.

(26) Gang, Y.; Li, B.; Fang, S.; Pellessier, J.; Fang, L.; Pan, F.; Du, Z.; Hang Hu, Y.; Li, T.; Wang, G.; et al. Efficient electrochemical CO<sub>2</sub> reduction to CO by metal and nitrogen co-doped carbon catalysts derived from pharmaceutical wastes adsorbed on commercial carbon nanotubes. *Chem. Eng. J.* **2023**, *453*, 139712.

(27) Chen, Y.; Zou, L.; Liu, H.; Chen, C.; Wang, Q.; Gu, M.; Yang, B.; Zou, Z.; Fang, J.; Yang, H. Fe and N Co-Doped Porous Carbon Nanospheres with High Density of Active Sites for Efficient CO<sub>2</sub> Electroreduction. *J. Phys. Chem. C* **2019**, *123* (27), 16651-16659.

(28) Gong, Y. N.; Jiao, L.; Qian, Y.; Pan, C. Y.; Zheng, L.; Cai, X.; Liu, B.; Yu, S. H.; Jiang, H. L. Regulating the Coordination Environment of MOF-Templated Single-Atom Nickel Electrocatalysts for Boosting CO<sub>2</sub> Reduction. *Angew. Chem.-Int. Ed.* **2020**, *59* (7), 2705-2709.

(29) Hu, X.-M.; Hval, H. H.; Bjerglund, E. T.; Dalgaard, K. J.; Madsen, M. R.; Pohl, M.-M.; Welter, E.; Lamagni, P.; Buhl, K. B.; Bremholm, M.; et al. Selective CO<sub>2</sub> Reduction to CO in Water using Earth-Abundant Metal and Nitrogen-Doped Carbon Electrocatalysts. *ACS Catal.* **2018**, *8* (7), 6255-6264.